Electronic Structure and Photophysics of Low Spin d^5 Metallocenes

*Ann Marie May,[§] Mawuli Deegbey,[†] Kedy Edme,[§] Katherine J. Lee,[§] Robin N. Perutz,[‖] Elena Jakubikova,[†] and Jillian L. Dempsey[§]**

[§]Department of Chemistry, University of North Carolina at Chapel Hill, Chapel Hill, North Carolina, 27599-3290, United States

[†]Department of Chemistry, North Carolina State University, Raleigh, North Carolina, 27695, United States

[‖]Department of Chemistry, University of York, Heslington, York, YO10 5DD, United Kingdom

Metallocenes, Ligand-to-Metal Charge Transfer, Photophysics, Excited States, Time-dependent Density Functional Theory, Excited State Reduction Potential

ABSTRACT

The electronic structure and photophysics of two low spin metallocenes, decamethylmanganocene ($MnCp^*_2$) and decamethylrhenocene ($ReCp^*_2$), were investigated to probe their promise as photoredox reagents. Computational studies support the assignment of $^2E_2$ ground state configurations and low energy ligand-to-metal charge transfer transitions for both complexes. Weak emission is observed at room temperature for $ReCp^*_2$ with τ = 1.8 ns in pentane,

whereas $MnCp^*_2$ is not emissive. Calculation of the excited state reduction potentials for both metallocenes reveal their potential potency as excited state reductants ($E^{o\prime}([MnCp^*_2]^{+/0*}) = –2.90$ V and $E^{o\prime}([ReCp^*_2]^{+/0*}) = –2.61$ V vs. $Fc^{+/0}$). Comparatively, both complexes exhibit mild potentials for photo-oxidative processes ($E^{o\prime}([MnCp^*_2]^{0*/–}) = 0.30$ V and $E^{o\prime}([ReCp^*_2]^{0*/–}) = –0.20$ V vs. $Fc^{+/0}$). These results showcase the rich electronic structure of low spin d^5 metallocenes and their promise as excited state reductants.

Introduction

Metallocenes have a rich history as single electron transfer reagents and redox mediators.[1–9] Their utility stems from the accessibility of several metal-centered oxidation states and the stability of their anionic, neutral, and/or cationic forms.[2,4,10–17] Furthermore, their absorption profiles are largely dependent on their oxidation state and exhibit a variety of low energy optical transitions comprised of d–d, metal-to-ligand charge transfer (MLCT) and/or ligand-to-metal charge transfer (LMCT) excited states.[18–20] In many cases, these distinctive absorption profiles are exploited to monitor single electron transfer reactions, as oxidized and reduced metallocenes result in discrete color changes.[5,19,21-23]

Despite the strong absorbance features of metallocenes, the majority of metallocene reactivity studies have been relegated to ground state processes. However, some reports describe photo-initiated reactivity of metallocenes. For instance, ferrocene, titanocene, and zirconocene derivatives are known to initiate photoisomerization and photopolymerization reactions, and cobaltocene was recently shown to undergo photoinduced radical chemistry to facilitate catalytic reactions, such as cyclotrimerizations.[19,24-27] However, these reactions are typically driven by high energy light to promote ligand dissociation and generate reactive radical species capable of ground

state reactivity and/or catalysis. Owing to the rich excited state electronic structure of metallocenes, a wide array of excited state reactivity may be accessible from these complexes, enabling new photocatalytic scaffolds to drive challenging uphill reactions. In order to realize new photoreactivity from metallocenes, it is crucial to understand their electronic structure. In this study, we explore the electronic structure of two d^5 metallocenes, decamethylmanganocene ($MnCp^*_2$) and decamethylrhenocene ($ReCp^*_2$), using a combination of spectroscopy, electrochemistry, and time-dependent density functional theory (TD-DFT). These metallocenes were selected because they exhibit several promising characteristics that may enable photochemical reactions. First, despite their 17 e^- configurations, both metallocenes are known to exhibit chemical stability and exist in monomeric forms, unlike less bulky d^5 metallocenes like $ReCp_2$, where Cp = cyclopentadienyl.[17,28] Second, $ReCp^*_2$ has a low energy LMCT excited state, and we hypothesized $MnCp^*_2$ would exhibit a similar electronic transition due to its isoelectronic structure.[20] Consequently, the population of a metal-based bonding orbital via LMCT may facilitate a variety of photochemical reactions while maintaining the metallocene's chemical stability. Lastly, several oxidation states of these d^5 metallocenes are known, showcasing their potential to stabilize new photoproducts, especially those generated from excited state electron transfer reactions.[10–17]

Through experiment and computation, we herein provide a detailed analysis of the electronic structure and accessible excited states. There are three possible electronic configurations of d^5 metallocenes with D_5 symmetry: $^2A_1$, $^2E_2$ and $^6A_1$ (see **Figure 1**).[18,20,29] Many d^5 metallocenes have high spin $^6A_1$ configurations, including manganocene and several of its derivatives, whereas others exhibit low spin $^2A_1$ or $^2E_2$ configurations, with the $^2A_1$ state favored for larger ligand field splitting.[10,18,20,30,31] Notably, members of the manganocene family exhibit a ground state electronic

configuration that is highly sensitive to the substitution of the cyclopentadienyl ring and most are susceptible to spin crossover with external stimuli, indicating a delicate balance of steric and electronic effects that influence the ligand field splitting.[32-36] $^2E_2$ ground states have previously been assigned for the targeted metallocenes of this study, $MnCp^*_2$ and $ReCp^*_2$, as supported by magnetic susceptibility, magnetic circular dichroism (MCD), photoelectron spectroscopy, and electron paramagnetic resonance (EPR) measurements.[10,11,20] Our studies aimed to corroborate these claims and further visualize the donor and acceptor orbitals and their relative ordering, key considerations for future photochemical applications. In addition, we quantify both ground state and excited state thermochemical parameters relevant for driving photochemical reactions. Collectively, these data provide critical information to guide the exploration of d^5 metallocene photochemistry.

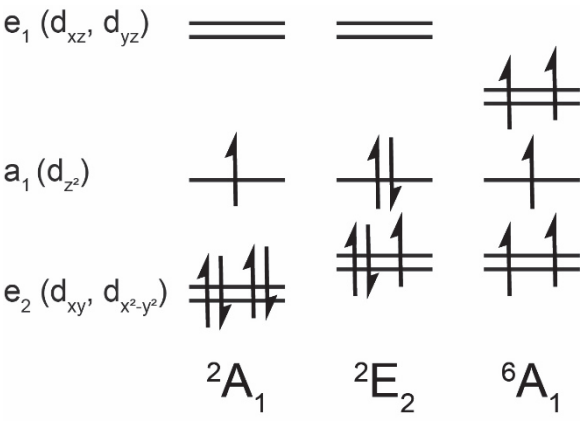

Figure 1. Possible electronic configurations of d^5 metallocenes, including $MnCp^*_2$ and $ReCp^*_2$.

Experimental

General considerations

All experiments were conducted under N_2 using standard high-vacuum Schlenk line and/or glovebox techniques unless otherwise noted. Acetonitrile (Thermo Fisher Scientific, HPLC grade, ≥ 99.9%), dichloromethane (Sigma-Aldrich ≥ 99.8%), tetrahydrofuran (Thermo Fisher Scientific, HPLC grade ≥ 99.9%), diethyl ether (Thermo Fisher Scientific, HPLC grade ≥ 99.9%), toluene (VWR, ACS reagent), and pentane (Thermo Fisher Scientific, HPLC grade ≥ 99%) were purified and degassed with argon using a Pure Process Technology solvent system. Benzene (VWR, anhydrous, 99.8%) and *N*,*N*-dimethylformamide (Sigma-Aldrich, anhydrous, 99.8%) were purchased and used as is without further purification. Deuterated toluene-d_8 (99.5%) was purchased from Cambridge Isotope Laboratories and dried with molecular sieves overnight. Tetrabutylammonium hexafluorophosphate ([Bu_4N][PF_6], Oakwood Chemical, 98%) was recrystallized twice from hot ethanol, dried under vacuum, and stored under a N_2-atmosphere. Decamethylmanganocene (Sigma Aldrich or Alfa Aesar) was dissolved in pentane, filtered, and the supernatant dried under vacuum prior to use. Decamethylrhenocene hydride was synthesized via metal vapor synthesis, whereupon vaporized rhenium was co-condensed with 1,2,3,4,5-pentamethylcyclopentadiene and purified by sublimation, following reported methods.[12] Decamethylrhenocene was synthesized by photolyzing decamethylrhenocene hydride (400 μg, 1 μmol, yellow) in pentane (5 mL) using a UV lamp under N_2 for ~60 hr, as described in literature.[12] Photolyses were conducted in a 1 cm path length custom quartz cuvette fitted with a Kontes valve to maintain a constant N_2 atmosphere. Reaction progress was monitored via UV-vis absorption spectroscopy (λ_{max} = 572 nm for $ReCp^*_2$) and full conversion was assumed when no additional spectral changes were observed over several hours. ^{1}H NMR spectra were obtained using a Bruker NEO 400 MHz spectrometer with a Prodigy probe. ^{1}H NMR chemical shifts were referenced to residual proteo-solvent peaks.

Spectroscopic measurements

All spectroscopic samples were prepared in an N_2-filled glovebox and transferred to a 1 cm path length custom quartz cuvette fitted with Kontes valve to maintain an inert atmosphere, unless otherwise specified. UV-vis absorption measurements were obtained at room temperature using an Agilent Cary 60 UV-vis absorption spectrophotometer. To determine the extinction coefficient of $ReCp^*_2$, absorption spectra were recorded in a screwtop 1 cm path length quartz cuvette within a N_2-filled glovebox using fiber optic cables coupled to the Agilent Cary 60 UV-vis absorption spectrophotometer. All other absorption measurements were conducted using a quartz cuvette fitted with a Kontes valve. Steady-state photoluminescence spectra were obtained using a homebuilt fluorometer consisting of an Ocean Optics LLS LED excitation source (455 nm) fiber-coupled to an Ocean Optics CUV-UV-FL sample compartment and fiber-coupled to an Ocean Optics USB 2000 Spectrometer. Emission intensities at each wavelength were corrected for nonlinear spectrometer response. Time-correlated single photon counting (TCSPC) measurements were conducted using an Edinburgh FLS920 equipped with a 444.2 nm diode laser operated at 10 MHz repetition rate (Edinburgh Instruments EPL-445, 73 ps FWHM pulse width). UV photolyses were conducted using a ThorLabs M340L4 mounted LED at maximum power (340 nm, 53 mW min, 700 mA) controlled by a ThorLabs LED driver (T-Cube LEDD1B, 1200 mA max drive current) or Ocean Optics LLS LED excitation source (365 nm) fiber-coupled to an Ocean Optics CUV-UV-FL sample compartment.

Electrochemical measurements

Electrochemical measurements were performed at room temperature in a nitrogen-filled glovebox with a WaveDriver potentiostat (Pine Research) in tetrahydrofuran. Cyclic

voltammograms were obtained using either a 1 mm glassy carbon working electrode and 3 mm glassy carbon counter electrode or using a honeycomb Pt electrode with screenprinted counter electrode (Pine Research). All measurements employed a pseudo reference electrode. For measurements conducted with the 1 mm glassy carbon working electrode setup, a silver wire was submerged into an electrolyte-filled glass tube (0.25 M or 0.5 M $[Bu_4N][PF_6]$ depending on the experiment) fitted with a porous glass (Vycor) tip. For measurements conducted with the honeycomb working electrode, the silver wire reference electrode was not separated from bulk solution. Experiments using the glassy carbon working electrode utilized a 20 mL scintillation vial as an electrochemical cell and fitted with a custom-made Teflon cap to hold the three electrodes or a cuvette; measurements with the honeycomb working electrode utilized a custom 2 mm path length cuvette fitted with a custom electrode card & cap assembly to hold each electrode. In the glovebox, electrode leads were connected to the WaveDriver with a custom shielded electrode cable feedthrough. All scans were referenced to the ferrocenium/ferrocene couple at 0 V using ferrocene as the internal standard (0 V vs. $Fc^{+/0}$). Ohmic drop was minimized by using a high electrolyte concentration (0.25 M or 0.5 M $[Bu_4N][PF_6]$), as well as by minimizing the distance between the working and reference electrodes. Residual ohmic drop was compensated using the positive feedback uncompensated resistance method (Pine Research). Glassy carbon electrodes (CH Instruments) were polished with 0.05 μm alumina powder (CH Instruments, contained no agglomerating agents) in Milli-Q water slurries, rinsed with Milli-Q water and briefly ultrasonicated in Milli-Q water to remove residual polishing powder. The glassy carbon working electrode was pretreated with cyclical scans from approximately 1 V to –2.5 V (referenced to the silver wire pseudo-reference) at 250 mV/s in 0.25 M $[Bu_4N][PF_6]$ until cycles were superimposable (~3 cycles). The Pt honeycomb electrode was cleaned with 0.5 M H_2SO_4 and

electrochemically cycled from –0.3 V to 1.7 V at 500 mV/s (≥ 20 cycles) and rinsed with DI water following each use.

Computational Details

All calculations were carried out using the B3LYP[37,38] functional and Grimme's D3 dispersion correction.[39] The 6-311G* basis set was used for all ligand atoms (H, C)[40,41] and the SDD basis sets with their accompanying pseudopotentials and an additional f polarization function were used for Mn and Re.[42-44] Geometry optimizations were performed on all structures in tetrahydrofuran (THF) and toluene followed by frequency calculations to ensure that all optimized structures were true minima with no imaginary frequencies. Starting geometries (and coordinates) for optimization were taken from the experimental crystal structures.[20,45] TD-DFT was employed to simulate absorption spectra utilizing the same model chemistry as structure optimizations. The implicit polarizable continuum solvation model (PCM)[46] for THF and toluene was used both for structure optimizations and excited state calculations to compare with experimental spectra. Eighty lowest-energy excited states were calculated for the doublet states of Mn(II) and Re(II) via TD-DFT. The calculated UV-Vis absorption spectra were obtained by broadening the stick spectra using Lorentzian functions with a half-width at half-maximum of 0.33 eV. All calculations were carried out using the Gaussian 16 software package.[47] Mulliken population analysis was performed to determine the percent compositions of molecular orbitals (MO) between the fragments using the AOMix software.[48,49]

In addition to the calculations presented here, we have performed several benchmarking studies utilizing the OPBE functional to determine the functional dependence of geometrical parameters and excited state properties for each metallocene. Although there are some differences in the

results obtained with the two different functionals, they do provide the same qualitative picture for the electronic structure and excited-state properties of the two metallocenes. The results of these calculations are discussed in the Supporting Information.[44]

Results & Discussion

Ground State Electronic Structure

Unrestricted DFT calculations were carried out to elucidate the ground state electronic structure of $MnCp^*_2$ and $ReCp^*_2$ in toluene. Optimized structures show that the Cp* ligands of $MnCp^*_2$ are offset by a torsion angle of 17.90° and are consistent with other computational reports of manganocene derivatives,[32] whereas the Cp* ligands of $ReCp^*_2$ are eclipsed (torsion angle is 4.39°). Single crystal X-ray diffraction studies further support these calculations, as $MnCp^*_2$ adopts a staggered conformation with Mn–C distances ranging from 2.105 Å – 2.118 Å,[45] while $ReCp^*_2$ has an eclipsed conformation and its Re–C bond lengths are significantly longer (2.223 Å – 2.238 Å) in the solid state.[20] The staggered conformation observed for $MnCp^*_2$ is likely driven by steric interactions between the methyl substituents in the abutting Cp* ligands. Qualitative d-orbital splitting diagrams for $ReCp^*_2$ and $MnCp^*_2$ are plotted in **Figure 2** based on these calculations. In comparison to the frontier molecular orbital diagrams presented in **Figure 1**, these calculations show a break in degeneracy of the e_2 (d_{xy} and $d_{x^2-y^2}$) and e_1 (d_{xz} and d_{yz}) orbitals. This break in degeneracy can be attributed to the unrestricted nature of this calculation, where alpha and beta electron spins are independently calculated, whereas degeneracy of spins is assumed in the construction of the frontier MO diagrams in **Figure 1**. Please note that our electronic structure calculations do not account for spin-orbit coupling effects, which impacts the calculated energetics

of the different spin-states. Our calculated MO diagrams in **Figure 2** indicate $^2E_2$ ground states for both metallocenes, in agreement with previous experimental studies discussed above.[10,11,20]

When comparing the calculated molecular orbital diagrams for $ReCp^*_2$ and $MnCp^*_2$, we note differences between the relative energetics of the d_z^2 and d_{xy} orbitals. For $ReCp^*_2$, the d_z^2 orbital is higher in energy than the d_{xy} orbital, while the converse is true for $MnCp^*_2$. Further, the unoccupied $d_{x^2-y^2}$ orbital is lower in energy for $ReCp^*_2$ than $MnCp^*_2$. The orbital energetics are underpinned by differences in orbital overlap arising from the disparate size of Re 5d vs. Mn 3d orbitals and the eclipsed vs. staggered conformations of the two metallocenes.[50]

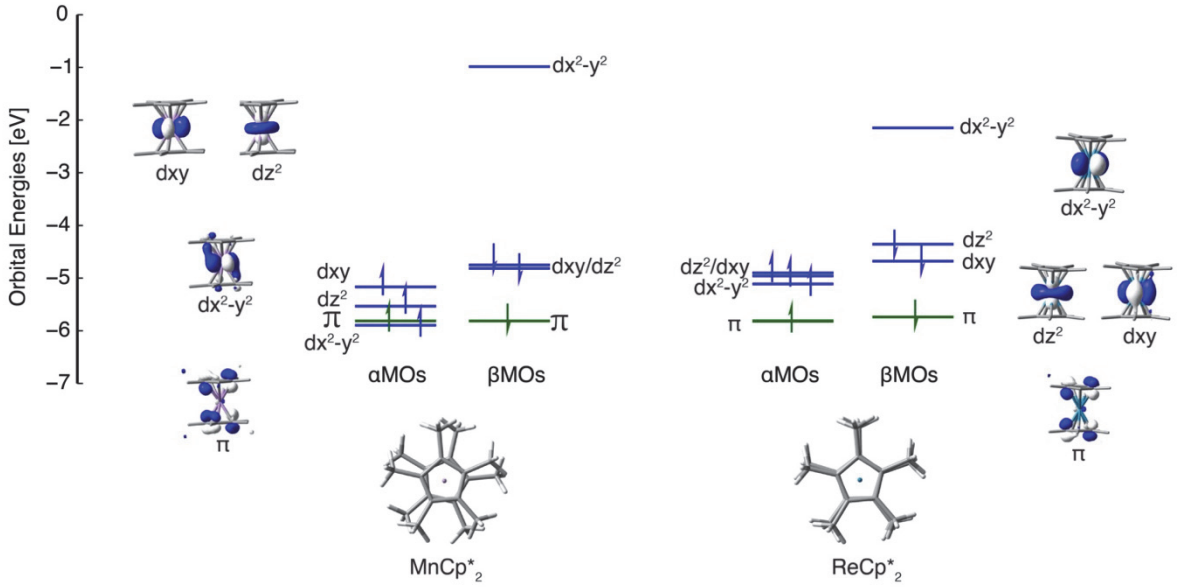

Figure 2. Qualitative MO diagram for $MnCp^*_2$ and $ReCp^*_2$ complexes. π label depicts the highest occupied ligand-based π orbitals. Color codes: blue represents metal d-orbitals and green ligand π-orbitals.

Absorption Spectra

Previous studies have reported the brilliant orange and dark purple colors of $MnCp^*_2$ and $ReCp^*_2$, respectively.[10,12,20] The absorption spectra (**Figure 3**) of these complexes in pentane reveal three prominent features: a broad, low energy feature, a low intensity feature at slightly higher energy, and an intense feature within the ultraviolet region. For $MnCp^*_2$, these features are centered at 468 nm (ε_{468} = 1047 ± 16 $M^{-1}cm^{-1}$), 380 nm (ε_{380} = 364 ± 6 $M^{-1}cm^{-1}$), and 342 nm (ε_{342} = 2855 ± 44 $M^{-1}cm^{-1}$), respectively. Comparatively, the two analogous low energy features of $ReCp^*_2$ are bathochromically shifted (λ_{max} = 572 nm, ε_{572} = 1055 ± 16 $M^{-1}cm^{-1}$ and λ_{max} = ~475 nm, ε_{475} = 202 ± 3 $M^{-1}cm^{-1}$) and the highest energy absorption feature is hypsochromically shifted (λ_{max} = ~300 nm).

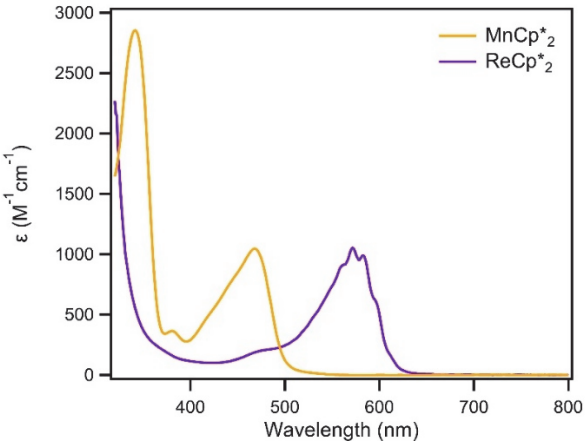

Figure 3. UV-vis absorption spectra of $MnCp^*_2$ (orange) and $ReCp^*_2$ (purple) in pentane.

Perutz and coworkers assigned the broad low energy feature of $ReCp^*_2$ ($\lambda_{max, exp}$ = 572 nm) as a LMCT transition.[20] This assignment stems from the literature precedence of LMCT excited states for 17 e^- metallocenes and the temperature dependent vibrational fine structure observed for $ReCp^*_2$, which sharpens upon cooling.[20] As noted above, the absorption spectrum of $MnCp^*_2$ is similar to that of $ReCp^*_2$. Both have low energy, asymmetric features with similar profiles, but to our knowledge the optical transitions of $MnCp^*_2$ have not been previously assigned. To further

interrogate the optical profiles of the two metallocenes, we employed TD-DFT to characterize their optical transitions by visual inspection of hole-particle pairs with large extinction coefficients adding up to at least 80% of the excited state contributions, **Figure 4**.

Computational studies first aimed to investigate $ReCp^*_2$ and further support the assignment of the low energy absorption feature to a LMCT transition. In agreement with experiment, a low energy peak at 508 nm is predicted, corresponding to donation from Cp* ligand π-orbitals (MO 79b and 80b) to a Re d-orbital (MO 83b), **Figure 5B**. In addition to this low energy LMCT excited state, a variety of other higher-energy excited states are also predicted within the UV region, consistent with the observed spectral profile of $ReCp^*_2$. The vibrational fine structure known for this complex is not conveyed within its calculated absorption spectra, as only electronic excitations were calculated. Interestingly, both low energy transitions exhibit 99% LMCT character, uncharacteristic of previously reported rhenium(II) complexes where metal-ligand mixing is more prevalent.[51,52] Solvatochromism was similarly not observed for this complex across four solvents (dielectric constants ranging from 1.8 – 8.9),[53–55] further supporting the presence of highly symmetric LMCT excited states (**Figures S5-S6**).[52]

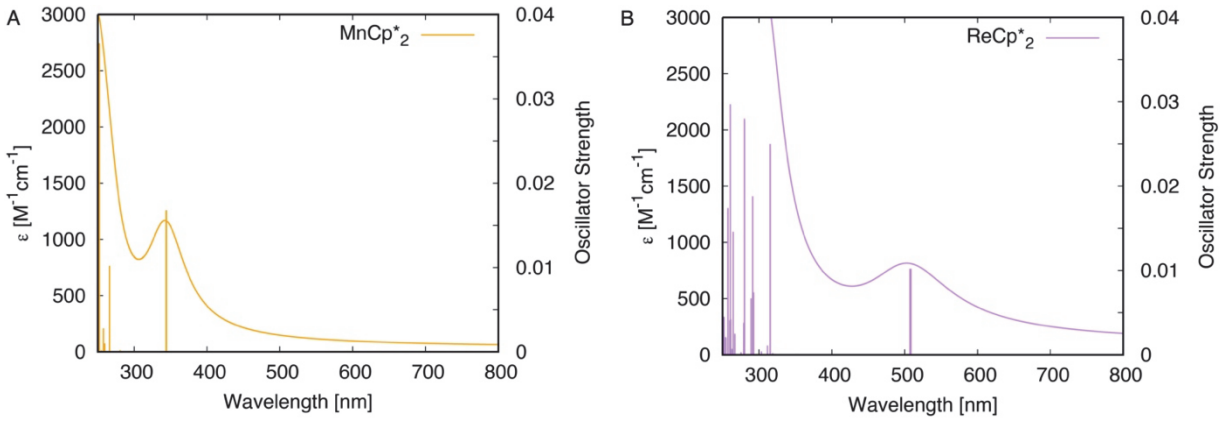

Figure 4. Calculated UV-vis absorption spectra of A) $MnCp^*_2$ and B) $ReCp^*_2$ in THF at B3LYP+D3/6-311G*,SDD+f(Mn,Re) level of theory.

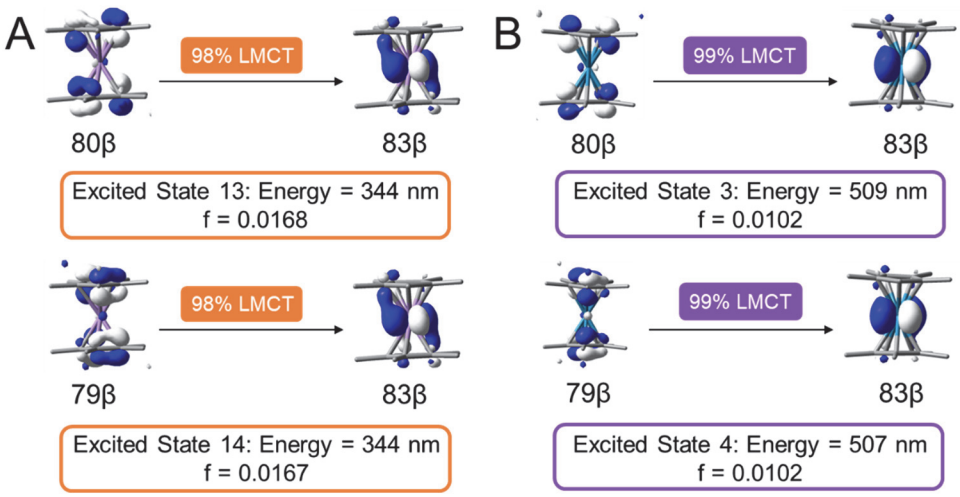

Figure 5. Donor and acceptor orbitals of the lowest energy excited states for A) $MnCp^*_2$ and B) $ReCp^*_2$. Excited states are numbered based on their relative energies. Calculated energies and oscillator strengths (f) for each electronic transition are also provided. The percent contribution of the displayed hole-particle pair was determined from the excitation coefficients obtained from the TD-DFT calculations.

The optical transitions that dominate the UV-vis absorption spectrum of $MnCp^*_2$ are similar to those quantified for $ReCp^*_2$ (**Figure 5A**) The lowest energy absorption feature at 468 nm is attributed to two excited states (13 & 14), consisting of electron transfer from Cp*(π)-based molecular orbitals (MO 79b and 80b) to a Mn d-orbital (MO 83b). These transitions exhibit 98% LMCT character, showcasing minimal metal-orbital mixing (consistent with the results of $ReCp^*_2$). Solvatochromism studies across eight solvents (dielectric constants ranging from 1.8 – 38.5)[53–59] also did not reveal any solvent-dependent spectral shifts, further supporting the presence of low energy LMCT excited states with high symmetry (**Figures S11-12**). Higher energy transitions in the UV region are also predicted for $MnCp^*_2$, further rationalizing its absorption

profile. Calculations obtained with the B3LYP functional predict the LMCT transitions are centered at λ_{max} = 344 nm, hypsochromically shifted (~120 nm) from the experimental spectrum.

Photoluminescence Measurements

Upon irradiation of $ReCp^*_2$ in toluene at 568 nm, broad emission is observed at room temperature ($\lambda_{max,em}$ = 641 nm), consistent with previous low temperature photoluminescence measurements (**Figure 6**).[20,60,61] Monitoring the emission of this compound at 641 nm reveals a room temperature lifetime of 1.8 ns in pentane, compared to 3.69 ns in a N_2 matrix at 12 K.[60] This lifetime, together with the almost perfect overlap of the (0,0) component in absorption and emission in a low temperature matrix, is consistent with fluorescence from a ^{2}LMCT excited state.[20] By contrast, no emission is detected for $MnCp^*_2$. This observation is rationalized by the relative ordering of the LMCT excited states with respect to other optical transitions. For $ReCp^*_2$, two excited states (d–d transitions) are predicted to lie at lower energies than the LMCT, whereas $MnCp^*_2$ is predicted to exhibit twelve lower-lying excited states, ten of which exhibit d–d character. These lower energy excited states are likely responsible for enabling non-radiative decay pathways under the room temperature conditions studied.[62]

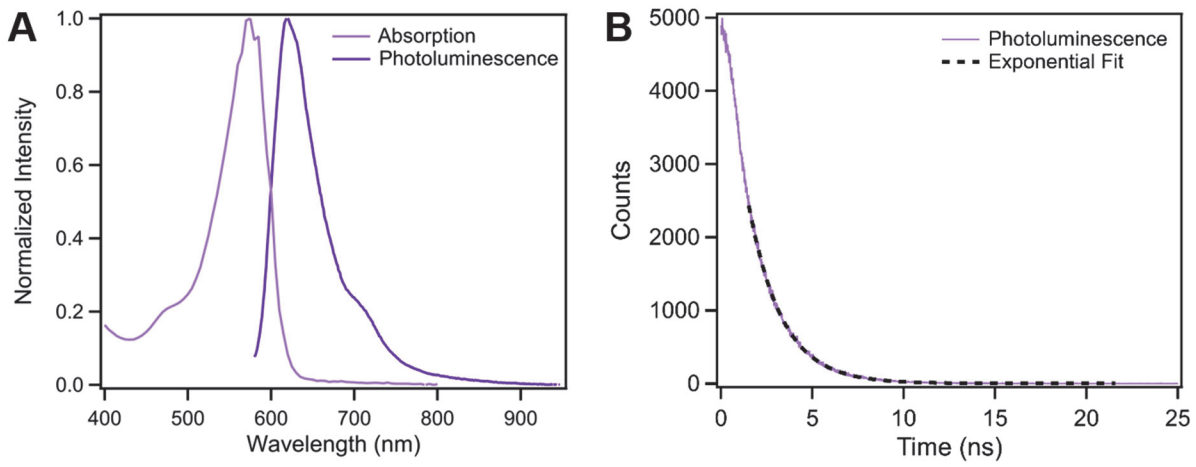

Figure 6. A) Normalized UV-vis absorption spectrum overlaid with the steady state photoluminescence spectrum (λ_{ex} = 568 nm) of $ReCp^*_2$ in toluene. B) Time-correlated single photon counting kinetic trace of $ReCp^*_2$ monitored at 641 nm (λ_{ex} = 568 nm), revealing τ = 1.8 ns.

Excited State Reduction Potentials

Driven by the strong absorption of these compounds in the visible region, we aimed to explore the utility of these metal complexes as photosensitizers by determining their excited state reduction potentials. The cyclic voltammogram of $MnCp^*_2$ in THF contains two one-electron redox couples (**Figure 7)**, assigned as the $[MnCp^*_2]^{+/0}$ couple ($E^{o'}$ = –0.43 V vs. $Fc^{+/0}$) and the $[MnCp^*_2]^{0/-}$ couple ($E^{o'}$ = –2.17 V vs. $Fc^{+/0}$). This observation is aligned with previous reports that $MnCp^*_2$ is stable in three oxidation states ($[MnCp^*_2]^-$, $MnCp^*_2$, and $[MnCp^*_2]^+$) in CH_3CN.[10] The cyclic voltammogram of $ReCp^*_2$ in THF similarly exhibits two reversible redox features, which we assign as the $[ReCp^*_2]^{+/0}$ couple ($E^{o'}$ = –0.54 V vs. $Fc^{+/0}$) and the $[ReCp^*_2]^{0/-}$ couple ($E^{o'}$ = –2.27 V vs. $Fc^{+/0}$) (**Figure 8**).

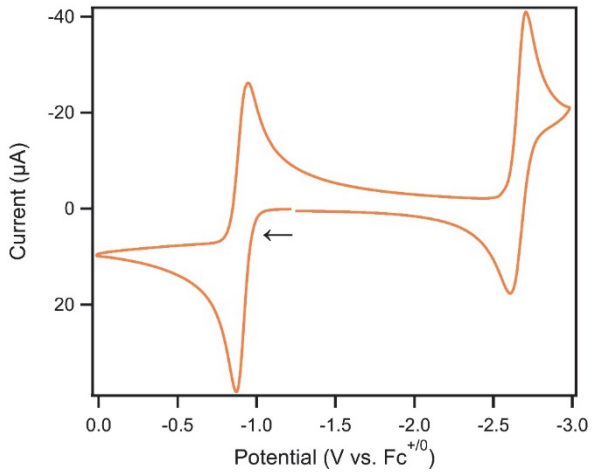

Figure 7. Cyclic voltammogram of 3 mM $MnCp^*_2$ in THF (orange). The voltammogram was recorded at 50 mV/s in 0.25 M $[NBu_4]PF_6$ THF solution under a N_2 atmosphere with a 1 mm

diameter glassy carbon working electrode, a 3 mm diameter glassy carbon counter electrode (in the same compartment as the working electrode), and a silver wire pseudo-reference electrode. Voltammogram is referenced to ferrocene using a ferrocene internal reference. Applied voltage is corrected for ohmic drop using a positive feedback uncompensated resistance (Pine Research). Voltammograms are plotted in polarographic convention; arrow shows starting point and direction of scan.

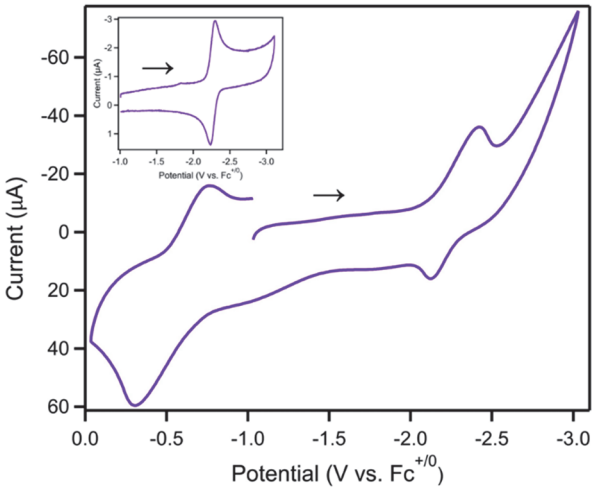

Figure 8. Cyclic voltammogram of $ReCp^*_2$ in THF (purple). The voltammogram was recorded at 50 mV/s in 0.5 M $[NBu_4]PF_6$ THF solution under a N_2 atmosphere using a platinum honeycomb working electrode and silver pseudoreference. Voltammogram is referenced to ferrocene using a ferrocene internal reference. The large peak-to-peak separation in this voltammogram arises from the use of the non-planar honeycomb electrode which imparts additional resistance. The inset includes an additional cyclic voltammogram, highlighting the reversibility of the $Re^{II/I}$ redox couple. This voltammogram was recorded at 50 mV/s in 0.5 M $[NBu_4]PF_6$ THF solution under a N_2 atmosphere with a 1 mm diameter glassy carbon electrode, a 3 mm diameter glassy carbon electrode (unseparated from the working electrode), and a silver wire pseudo-reference electrode. Voltammogram is referenced to ferrocene using a ferrocene internal reference. Applied voltage is

corrected for ohmic drop using a positive feedback uncompensated resistance (Pine Research). Voltammograms are plotted in polarographic convention; arrow shows starting point and direction of scan.

Upon determination of ground state reduction potentials for both complexes, their excited state reduction potentials were calculated using **Eq 1 and 2** where M = Re or Mn.[63] For $ReCp^*_2$, the free energy stored in the excited state (ΔG_{ES}) was estimated from the crossing point of its absorption and steady state emission profiles at room temperature (600 nm, 2.07 eV, **Figure 6**). As mentioned above, $MnCp^*_2$ was found to exhibit no room temperature photoluminescence. Therefore, its ΔG_{ES} value was estimated from a tangent line drawn on the low-energy side of the LMCT absorption band (501 nm, 2.47 eV, see **Figure S10**).[64] **Figure 9** summarizes the ground state reduction potentials, free energy stored in the excited state, and excited state reduction potentials for both decamethylmetallocenes in the form of a modified Latimer diagram.

$$E^{o'}([MCp^*_2]^{+/0*}) = E^{o'}([MCp^*_2]^{+/0}) - \Delta G_{ES} \quad (1)$$

$$E^{o'}([MCp^*_2]^{0*/-}) = E^{o'}([MCp^*_2]^{0/-}) + \Delta G_{ES} \quad (2)$$

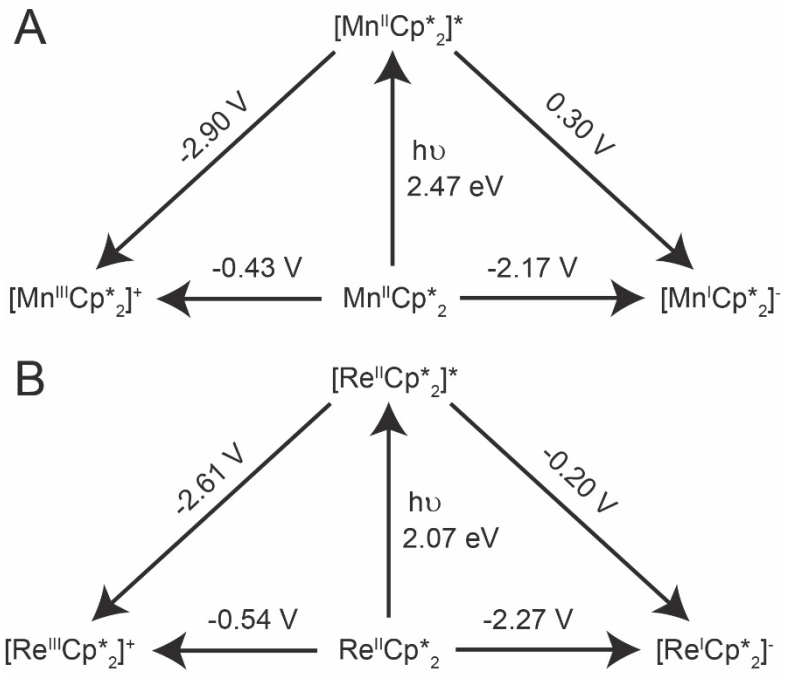

Figure 9. Modified Latimer diagrams of A) MnCp*$_2$ and B) ReCp*$_2$. All potentials are referenced vs. $Fc^{+/0}$.

The excited state reduction potentials of MnCp*$_2$ are calculated to be 0.30 V and –2.90 V vs. $Fc^{+/0}$ for the $[MnCp^*_2]^{0*/-}$ and $[MnCp^*_2]^{+/0*}$ couples, respectively. The excited state reduction potentials are similar for ReCp*$_2$ where the $E^{o'}([ReCp^*_2]^{0*/-})$ is –0.20 V and $E^{o'}([ReCp^*_2]^{+/0*})$ is –2.61 V vs. $Fc^{+/0}$. For comparison, $[Ru(bpy)_3]^{2+}$ (bpy = 2,2′-bipyridine), exhibits potentials of 0.37 V and –1.21 V vs. $Fc^{+/0}$ for the $[Ru(bpy)_3]^{2+*/+}$ and $[Ru(bpy)_3]^{3+/2+*}$ couples in CH_3CN, respectively.[63,65] ReCp*$_2$ and MnCp*$_2$ exhibit mild excited state reduction potentials for photo-oxidative processes, but much stronger excited state reduction potentials for photo-reductive processes than $[Ru(bpy)_3]^{2+}$. These results showcase the strongly reducing power of the LMCT excited states for both MnCp*$_2$ and ReCp*$_2$. Furthermore, ReCp*$_2$ exhibits a sufficient lifetime for bimolecular reactivity[66–68] and ongoing studies are investigating its excited state reactivity, where its potency as a photoreductant can be further explored.

Conclusion

Understanding the electronic structure of light-absorbing transition metal complexes is essential to drive photochemical reactions. In this study, the electronic structure of two d^5 metallocenes, $MnCp^*_2$ and $ReCp^*_2$ were investigated and found to have $^2E_2$ ground states consistent with prior experimental reports. Electrochemical studies revealed Mn and Re have similar ground state reduction potentials for the $[MCp^*_2]^{+/0}$ and $[MCp^*_2]^{0/-}$ couples. By coupling these reduction potentials with additional photophysical data, the excited state reduction potentials in THF were determined. The excited state redox potentials of $MnCp^*_2$ were 0.30 V and –2.90 V vs. $Fc^{+/0}$ for the $[MnCp^*_2]^{0*/-}$ and $[MnCp^*_2]^{+/0*}$ couples, respectively. The excited state reduction potentials for $ReCp^*_2$ were –0.20 V and –2.61 V vs. $Fc^{+/0}$ for the $[ReCp^*_2]^{0*/-}$ and $[ReCp^*_2]^{+/0*}$ couples, respectively. These excited state reduction potentials suggest both metallocenes can serve as strong photoreductants, but weak photo-oxidants. Collectively, these studies showcase the excited state properties of $MnCp^*_2$ and $ReCp^*_2$ and their potential as potent excited state reductants.

ASSOCIATED CONTENT

Supporting Information. Photolysis; Beer-Lambert plots; ^1H NMR spectra; steady-state photoluminescence spectra; time-resolved photoluminescence measurements; cyclic voltammograms; solvatochromism measurements, and computational data.

The following files are available free of charge.

Supporting Information (PDF)

AUTHOR INFORMATION

Corresponding Author

Jillian L. Dempsey – *Department of Chemistry, University of North Carolina at Chapel Hill, Chapel Hill, North Carolina, 27599-3290;* Email: dempseyj@email.unc.edu

ACKNOWLEDGMENT

This work was supported by the National Science Foundation for both experimental (CHE-1954868) and theoretical (CHE-1554855) aspects of this project. A.M.M. acknowledges support from the Department of Defense through the National Defense Science & Engineering Graduate (NDSEG) Fellowship Program. We thank the University of North Carolina's Department of Chemistry NMR Core Laboratory for the use of their NMR spectrometers and Professor F. G. N. Cloke (Sussex) for the sample of decamethylrhenocene. We also acknowledge the use of the computing resources provided by North Carolina State University High Performance Computing Services Core Facility (RRID: SCR 022168).

ABBREVIATIONS

MLCT, metal-to-ligand charge transfer; LMCT, ligand-to-metal charge transfer; TD-DFT, time-dependent density functional theory; MCD, magnetic circular dichroism; EPR, electron paramagnetic resonance.

REFERENCES

(1) Elgrishi, N.; Rountree, K. J.; McCarthy, B. D.; Rountree, E. S.; Eisenhart, T. T.; Dempsey, J. L. A Practical Beginner's Guide to Cyclic Voltammetry. *J. Chem. Educ.* **2018**, *95* (2), 197–206. https://doi.org/10.1021/acs.jchemed.7b00361.

(2) Gagne, R. R.; Koval, C. A.; Lisensky, G. C. Ferrocene as an Internal Standard for Electrochemical Measurements. *Inorg. Chem.* **1980**, *19* (9), 2854–2855. https://doi.org/10.1021/ic50211a080.

(3) Fabbrizzi, L. The Ferrocenium/Ferrocene Couple: A Versatile Redox Switch. *ChemTexts* **2020**, *6* (4), 22. https://doi.org/10.1007/s40828-020-00119-6.

(4) Holloway, J. D. L.; Geiger, W. E. Jr. Electron-Transfer Reactions of Metallocenes. Influence of Metal Oxidation State on Structure and Reactivity. *J. Am. Chem. Soc.* **1979**, *101* (8), 2038–2044. https://doi.org/10.1021/ja00502a018.

(5) Connelly, N. G.; Geiger, W. E. Chemical Redox Agents for Organometallic Chemistry. *Chem. Rev.* **1996**, *96* (2), 877–910. https://doi.org/10.1021/cr940053x.

(6) Lee, K. J.; Lodaya, K. M.; Gruninger, C. T.; Rountree, E. S.; Dempsey, J. L. Redox Mediators Accelerate Electrochemically-Driven Solubility Cycling of Molecular Transition Metal Complexes. *Chem. Sci.* **2020**, *11* (36), 9836–9851. https://doi.org/10.1039/D0SC02592E.

(7) Chalkley, M. J.; Garrido-Barros, P.; Peters, J. C. A Molecular Mediator for Reductive Concerted Proton-Electron Transfers via Electrocatalysis. *Science* **2020**, *369* (6505), 850–854. https://doi.org/10.1126/science.abc1607.

(8) Zhang, Z.; Hilche, T.; Slak, D.; Rietdijk, N. R.; Oloyede, U. N.; Flowers II, R. A.; Gansäuer, A. Titanocenes as Photoredox Catalysts Using Green-Light Irradiation. *Angew. Chem. Int. Ed.* **2020**, *59* (24), 9355–9359. https://doi.org/10.1002/anie.202001508.

(9) Calogero, F.; Magagnano, G.; Potenti, S.; Pasca, F.; Fermi, A.; Gualandi, A.; Ceroni, P.; Bergamini, G.; Cozzi, P. G. Diastereoselective and Enantioselective Photoredox Pinacol Coupling

Promoted by Titanium Complexes with a Red-Absorbing Organic Dye. *Chem. Sci.* **2022**, *13* (20), 5973–5981. https://doi.org/10.1039/d2sc00800a.

(10) Robbins, J. L.; Edelstein, N. M.; Cooper, S. R.; Smart, J. C. Syntheses and Electronic Structures of Decamethylmanganocenes. *J. Am. Chem. Soc.* **1979**, *101* (14), 3853–3857. https://doi.org/10.1021/ja00508a023.

(11) Smart, J. C.; Robbins, J. L. A Low Spin Manganocene and Its Novel Anionic Derivative. Synthesis and Characterization of Decamethylmanganocene Complexes. *J. Am. Chem. Soc.* **1978**, *100* (12), 3936–3937. https://doi.org/10.1021/ja00480a051.

(12) Cloke, F. G. N.; Day, J. P. Synthesis of Bis(η-pentamethylcyclopentadienyl)rhenium Hydride and Its Photochemical Conversion into Decamethylrhenocene. *J. Chem. Soc. Chem. Commun.* **1985**, (14), 967–968. https://doi.org/10.1039/C39850000967.

(13) Goodwin, C. A. P.; Giansiracusa, M. J.; Greer, S. M.; Nicholas, H. M.; Evans, P.; Vonci, M.; Hill, S.; Chilton, N. F.; Mills, D. P. Isolation and Electronic Structures of Derivatized Manganocene, Ferrocene and Cobaltocene Anions. *Nat. Chem.* **2021**, *13* (3), 243–248. https://doi.org/10.1038/s41557-020-00595-w.

(14) Malischewski, M.; Adelhardt, M.; Sutter, J.; Meyer, K.; Seppelt, K. Isolation and Structural and Electronic Characterization of Salts of the Decamethylferrocene Dication. *Science* **2016**, *353* (6300), 678–682. https://doi.org/10.1126/science.aaf6362.

(15) Gardner, B. M.; McMaster, J.; Lewis, W.; Liddle, S. T. Synthesis and Structure of [{$N(CH_2CH_2NSiMe_3)_3$}$URe(H_5$-$C_5H_5)_2$]: A Heterobimetallic Complex with an Unsupported

Uranium–Rhenium Bond. *Chem. Commun.* **2009**, (20), 2851–2853. https://doi.org/10.1039/B906554G.

(16) Magnoux, C.; Mills, D. P. Metallocene Anions: From Electrochemical Curiosities to Isolable Complexes. *Eur. J. Inorg. Chem.* **2022**, *2022* (11). https://doi.org/10.1002/ejic.202101063.

(17) Pasman, P.; Snel, J. J. M. The Synthesis and Reactivity of Rhenocene. *J. Organomet. Chem.* **1984**, *276* (3), 387–392. https://doi.org/10.1016/0022-328X(84)80660-9.

(18) Gray, H. B.; Sohn, Y. S.; Hendrickson, N. Electronic Structure of Metallocenes. *J. Am. Chem. Soc.* **1971**, *93* (15), 3603–3612. https://doi.org/10.1021/ja00744a011.

(19) Bozak, R. E. Photochemistry in the Metallocenes. In *Advances in Photochemistry*; John Wiley & Sons, Ltd, 1971; pp 227–244. https://doi.org/10.1002/9780470133385.ch5.

(20) Bandy, J. A.; Cloke, F. G. N.; Copper, Glyn.; Day, J. P.; Girling, R. B.; Graham, R. G.; Green, J. C.; Grinter, Roger.; Perutz, R. N. Decamethylrhenocene, $(\eta^5\text{-}C_5Me_5)_2Re$. *J. Am. Chem. Soc.* **1988**, *110* (15), 5039–5050. https://doi.org/10.1021/ja00223a023.

(21) Paul, A.; Borrelli, R.; Bouyanfif, H.; Gottis, S.; Sauvage, F. Tunable Redox Potential, Optical Properties, and Enhanced Stability of Modified Ferrocene-Based Complexes. *ACS Omega* **2019**, *4* (12), 14780–14789. https://doi.org/10.1021/acsomega.9b01341.

(22) Ryan, O. B.; Tilset, M. Oxidation of $CpRu(CO)(PMe_3)H$ by 2/3, 1, and 2 Electrons by the Judicious Choice of Reaction Conditions. Generation of a Bridging Hydride via the Reaction between a 17-Electron Metal Hydride Cation Radical and Its Conjugate Base. *J. Am. Chem. Soc.* **1991**, *113* (25), 9554–9561. https://doi.org/10.1021/ja00025a020.

(23) Huang, T.; Rountree, E. S.; Traywick, A. P.; Bayoumi, M.; Dempsey, J. L. Switching between Stepwise and Concerted Proton-Coupled Electron Transfer Pathways in Tungsten Hydride Activation. *J. Am. Chem. Soc.* **2018**, *140* (44), 14655–14669. https://doi.org/10.1021/jacs.8b07102.

(24) Dannenberg, J. J.; Richards, J. H. Photosensitization by Ferrocene. Photochemistry of Higher Electronic Excited States. *J. Am. Chem. Soc.* **1965**, *87* (7), 1626–1627. https://doi.org/10.1021/ja01085a048.

(25) Harrigan, R. W.; Hammond, G. S.; Gray, H. B. Photochemistry of Titanocene(IV) Derivatives. *J. Organomet. Chem.* **1974**, *81* (1), 79–85. https://doi.org/10.1016/S0022-328X(00)87889-4.

(26) Prather, K. V.; Tsui, E. Y. Photoinduced Ligand-to-Metal Charge Transfer of Cobaltocene: Radical Release and Catalytic Cyclotrimerization. *Inorg. Chem.* **2023**, *62* (5), 2128–2134. https://doi.org/10.1021/acs.inorgchem.2c03779.

(27) Dumur, F. Recent Advances on Ferrocene-Based Photoinitiating Systems. *Eur. Polym. J.* **2021**, *147*, 110328. https://doi.org/10.1016/j.eurpolymj.2021.110328.

(28) Bünder, W.; Weiss, E. Die Kristallstruktur von Bis(cyclopentadienyl)mangan, Eine Polymere Verbindung Mit Cyclopentadienyl-Brücken /The Crystal Structure of Bis(cyclopentadienyl)manganese, a Polymeric Compound with Cyclopentadienyl Bridges. *Z. Naturforsch. B* **1978**, *33* (11), 1235–1237. https://doi.org/10.1515/znb-1978-1107.

(29) Clack, D. W.; Warren, K. D. Metal-Ligand Bonding in 3d Sandwich Complexes. In *Electrons and Transitions*; Structure and Bonding; Springer: Berlin, Heidelberg, 1980; pp 1–41. https://doi.org/10.1007/3-540-09787-2_1.

(30) Ammeter, J. H.; Bucher, R.; Oswald, N. High-Spin-Low-Spin Equilibrium of Manganocene and Dimethylmanganocene. *J. Am. Chem. Soc.* **1974**, *96* (25), 7833–7835. https://doi.org/10.1021/ja00832a049.

(31) Cloke, F. G. N.; Dix, A. N.; Green, J. C.; Perutz, R. N.; Seddon, E. A. Electron Spin Resonance and Photoelectron Studies of Neutral Bis(η-arene)metal Compounds (Metal = Ti, V, Nb, Ta, Mo, and W). *Organometallics* **1983**, *2* (9), 1150–1159. https://doi.org/10.1021/om50003a014.

(32) Cirera, J.; Ruiz, E. Electronic and Steric Control of the Spin-Crossover Behavior in $[(Cp^R)_2Mn]$ Manganocenes. *Inorg. Chem.* **2018**, *57* (2), 702–709. https://doi.org/10.1021/acs.inorgchem.7b02592.

(33) Walter, M. D.; Sofield, C. D.; Andersen, R. A. Spin Equilibria and Thermodynamic Constants for $(C_5H_4R)_2Mn$, R = H or Me, in Solid Solutions of Diamagnetic Diluents. *J. Organomet. Chem.* **2015**, *776*, 17–22. https://doi.org/10.1016/j.jorganchem.2014.10.032.

(34) Walter, M. D.; Sofield, C. D.; Booth, C. H.; Andersen, R. A. Spin Equilibria in Monomeric Manganocenes: Solid-State Magnetic and EXAFS Studies. *Organometallics* **2009**, *28* (7), 2005–2019. https://doi.org/10.1021/om800922j.

(35) Blümel, J.; Hofmann, P.; Köhler, F. H. NMR spectroscopy of paramagnetic complexes. Part 39—natural abundance ^{2}H NMR of paramagnetic sandwich compounds. *Magn. Reson. Chem.* **1993**, *31* (1), 2–6. https://doi.org/10.1002/mrc.1260310103.

(36) Hebendanz, Nikolaus.; Köhler, F. H.; Mueller, Gerhard.; Riede, Juergen. Electron Spin Adjustment in Manganocenes. Preparative, Paramagnetic NMR and X-ray Study on Substituent and Solvent Effects. *J. Am. Chem. Soc.* **1986**, *108* (12), 3281–3289. https://doi.org/10.1021/ja00272a023.

(37) Becke, A. D. Density-Functional Exchange-Energy Approximation with Correct Asymptotic Behavior. *Phys. Rev. A* **1988**, *38* (6), 3098–3100. https://doi.org/10.1103/PhysRevA.38.3098.

(38) Becke, A. D. A New Mixing of Hartree–Fock and Local Density-functional Theories. *J. Chem. Phys.* **1993**, *98* (2), 1372–1377. https://doi.org/10.1063/1.464304.

(39) Grimme, S.; Antony, J.; Ehrlich, S.; Krieg, H. A Consistent and Accurate Ab Initio Parametrization of Density Functional Dispersion Correction (DFT-D) for the 94 Elements H-Pu. *J. Chem. Phys.* **2010**, *132* (15), 154104. https://doi.org/10.1063/1.3382344.

(40) Krishnan, R.; Binkley, J. S.; Seeger, R.; Pople, J. A. Self-consistent Molecular Orbital Methods. XX. A Basis Set for Correlated Wave Functions. *J. Chem. Phys.* **2008**, *72* (1), 650–654. https://doi.org/10.1063/1.438955.

(41) McLean, A. D.; Chandler, G. S. Contracted Gaussian Basis Sets for Molecular Calculations. I. Second Row Atoms, Z=11–18. *J. Chem. Phys.* **2008**, *72* (10), 5639–5648. https://doi.org/10.1063/1.438980.

(42) Dolg, M.; Wedig, U.; Stoll, H.; Preuss, H. Energy-adjusted Ab Initio Pseudopotentials for the First Row Transition Elements. *J. Chem. Phys.* **1987**, *86* (2), 866–872. https://doi.org/10.1063/1.452288.

(43) Ehlers, A. W.; Böhme, M.; Dapprich, S.; Gobbi, A.; Höllwarth, A.; Jonas, V.; Köhler, K. F.; Stegmann, R.; Veldkamp, A.; Frenking, G. A Set of F-Polarization Functions for Pseudo-Potential Basis Sets of the Transition Metals Sc–Cu, Y–Ag and La–Au. *Chem. Phys. Lett.* **1993**, *208* (1), 111–114. https://doi.org/10.1016/0009-2614(93)80086-5.

(44) Handy, N. C.; Cohen, A. J. Left-Right Correlation Energy. *Mol. Phys.* **2001**, *99* (5), 403–412. https://doi.org/10.1080/00268970010018431.

(45) Freyberg, D. P.; Robbins, J. L.; Raymond, K. N.; Smart, J. C. Crystal and Molecular Structures of Decamethylmanganocene and Decamethylferrocene. Static Jahn-Teller Distortion in a Metallocene. *J. Am. Chem. Soc.* **1979**, *101* (4), 892–897. https://doi.org/10.1021/ja00498a017.

(46) Scalmani, G.; Frisch, M. J. Continuous Surface Charge Polarizable Continuum Models of Solvation. I. General Formalism. *J. Chem. Phys.* **2010**, *132* (11), 114110. https://doi.org/10.1063/1.3359469.

(47) Frisch, M. J.; Trucks, G. W.; Schlegel, H. B.; Scuseria, G. E.; Robb, M. A.; Cheeseman, J. R.; Scalmani, G.; Barone, V.; Petersson, G. A.; Nakatsuii, H.; Li, X.; Caricato, M.; Marenich, A. V.; Bloino, J.; Janesko, B. G.; Gomperts, R.; Mennucci, B.; Hratchian, H. P.; Ortiz, J. V.; Izmaylov, A. F.; Sonnenberg, J. L.; Williams-Young, D.; Ding, F.; Lipparini, F.; Egidi, F.; Goings, J.; Peng, B.; Petrone, A.; Henderson, T.; Ranasinghe, D.; Zakrzewski, V. G.; Gao, J.; Rega, N.; Zheng, G.; Liang, W.; Hada, M.; Ehara, M.; Toyota, K.; Fukuda, R.; Hasegawa, J.; Ishida, M.; Nakajima, T.; Honda, Y.; Kitao, O.; Nakai, H.; Vreven, T.; Throssell, K.; Montgomery, Jr., J. A.;

Peralta, J. E.; Ogliaro, F.; Bearpark, M. J.; Heyd, J. J.; Brothers, E. N.; Kudin, K. N.; Staroverov, V. N.; Keith, T. A.; Kobayashi, R.; Normand, J.; Raghavachari, K.; Rendell, A. P.; Burant, J. C.; Iyengar, S. S.; Tomasi, J.; Cossi, M.; Millam, J. M.; Klene, M.; Adamo, C.; Cammi, R.; Ochterski, J. W.; Martin, R. L.; Morokuma, K.; Farkas, O.; Foresman, J. B.; Fox, D. J. Gaussian 16 Revision C.01. **2016**.

(48) Gorelsky, S. I.; Lever, A. B. P. Electronic Structure and Spectra of Ruthenium Diimine Complexes by Density Functional Theory and INDO/S. Comparison of the Two Methods. *J. Organomet. Chem.* **2001**, *635* (1), 187–196. https://doi.org/10.1016/S0022-328X(01)01079-8.

(49) Gorelsky, S. I. AOMix Program.

(50) Heise, H.; Köhler, F. H.; Xie, X. Solid-State NMR Spectroscopy of Paramagnetic Metallocenes. *J. Magn. Reson.* **2001**, *150* (2), 198–206. https://doi.org/10.1006/jmre.2001.2343.

(51) Rodriguez, T. M.; Deegbey, M.; Chen, C.-H.; Jakubikova, E.; Dempsey, J. L. Isocyanide Ligands Promote Ligand-to-Metal Charge Transfer Excited States in a Rhenium(II) Complex. *Inorg. Chem.* **2023**, *62* (17), 6576-6585. https://doi.org/10.1021/acs.inorgchem.2c03193.

(52) Rodriguez, T. M.; Deegbey, M.; Jakubikova, E.; Dempsey, J. L. The Ligand-to-Metal Charge Transfer Excited State of $[Re(dmpe)_3]^{2+}$. *Photosynth. Res.* **2022**, *151* (2), 155–161. https://doi.org/10.1007/s11120-021-00859-7.

(53) Ritzoulis, G.; Papadopoulos, N.; Jannakoudakis, D. Densities, viscosities, and dielectric constants of acetonitrile + toluene at 15, 25, and 35 °C. *J. Chem. Eng. Data.* **1986**, *31* (2) 146-148 https://doi.org/10.1021/je00044a004.

(54) Mardolcar, U. V.; Nieto de Castro, C. A.; Santos, F. J. V. Dielectric Constant Measurements of Toluene and Benzene. *Fluid Phase Equilibria* **1992**, *79*, 255–264. https://doi.org/10.1016/0378-3812(92)85135-U.

(55) Brazier, D. W.; Freeman, G. R. The Effects of Pressure on the Density, Dielectric Constant, and Viscosity of Several Hydrocarbons and Other Organic Liquids. *Can. J. Chem.* **1969**, *47* (6), 893–899. https://doi.org/10.1139/v69-147.

(56) Corradini, F.; Marcheselli, L.; Tassi, L.; Tosi, G. Static Dielectric Constants of the *N,N*-Dimethylformamide/2-Methoxyethanol Solvent System at Various Temperatures. *Can. J. Chem.* **1992**, *70* (12), 2895–2899. https://doi.org/10.1139/v92-370.

(57) Metz, D. J.; Glines, A. Density, Viscosity, and Dielectric Constant of Tetrahydrofuran between -78 and 30° *J. Phys. Chem.* **1967**, *71* (4), 1158–1158. https://doi.org/10.1021/j100863a067.

(58) Wyman, J. Jr. Dielectric Constants: Ethanol—Diethyl Ether and Urea—Water Solutions between 0 and 50°. *J. Am. Chem. Soc.* **1933**, *55* (10), 4116–4121. https://doi.org/10.1021/ja01337a029.

(59) Rumble ed., J. R. *CRC Handbook of Chemistry and Physics*, 104th Edition (Internet Version 2023).; CRC Press/Taylor & Francis: Boca Raton, FL.

(60) Hill, J. N.; Perutz, R. N.; Tavender, S. M. Laser-Induced Fluorescence of Decamethylrhenocene in Low-Temperature Matrices. *J. Phys. Chem.* **1996**, *100* (3), 934–940. https://doi.org/10.1021/jp9518116.

(61) Bell, S. E. J.; Hill, J. N.; McCamley, Andrew.; Perutz, R. N. Laser-Induced Fluorescence of Reactive Metallocenes (η^5-$C_5H_5)_2M$ (M = Re, W, Mo) and (η^5-$C_5Me_5)_2Re$. *J. Phys. Chem.* **1990**, *94* (10), 3876–3878. https://doi.org/10.1021/j100373a004.

(62) McCusker, J. K. Electronic Structure in the Transition Metal Block and Its Implications for Light Harvesting. *Science* **2019**, *363* (6426), 484–488. https://doi.org/10.1126/science.aav9104.

(63) Bock, C. R.; Connor, J. A.; Gutierrez, A. R.; Meyer, T. J.; Whitten, D. G.; Sullivan, B. P.; Nagle, J. K. Estimation of Excited-State Redox Potentials by Electron-Transfer Quenching. Application of Electron-Transfer Theory to Excited-State Redox Processes. *J. Am. Chem. Soc.* **1979**, *101* (17), 4815–4824. https://doi.org/10.1021/ja00511a007.

(64) Liu, F.; Meyer, G. J. Remote and Adjacent Excited-State Electron Transfer at TiO_2 Interfaces Sensitized to Visible Light with Ru(II) Compounds. *Inorg. Chem.* **2005**, *44* (25), 9305–9313. https://doi.org/10.1021/ic0513336.

(65) Zhang, Y.; Lee, T. S.; Favale, J. M.; Leary, D. C.; Petersen, J. L.; Scholes, G. D.; Castellano, F. N.; Milsmann, C. Delayed Fluorescence from a Zirconium(IV) Photosensitizer with Ligand-to-Metal Charge-Transfer Excited States. *Nat. Chem.* **2020**, *12* (4), 345–352. https://doi.org/10.1038/s41557-020-0430-7.

(66) Kjær, K. S.; Kaul, N.; Prakash, O.; Chábera, P.; Rosemann, N. W.; Honarfar, A.; Gordivska, O.; Fredin, L. A.; Bergquist, K.-E.; Häggström, L.; Ericsson, T.; Lindh, L.; Yartsev, A.; Styring, S.; Huang, P.; Uhlig, J.; Bendix, J.; Strand, D.; Sundström, V.; Persson, P.; Lomoth, R.; Wärnmark, K. Luminescence and Reactivity of a Charge-Transfer Excited Iron Complex with Nanosecond Lifetime. *Science* **2019**, *363* (6424), 249–253. https://doi.org/10.1126/science.aau7160.

(67) Taniguchi, M.; Lindsey, J. S.; Bocian, D. F.; Holten, D. Comprehensive Review of Photophysical Parameters (ε, Φ_f, τ_s) of Tetraphenylporphyrin (H_2TPP) and Zinc Tetraphenylporphyrin (ZnTPP) – Critical Benchmark Molecules in Photochemistry and Photosynthesis. *J. Photochem. Photobiol. C Photochem. Rev.* **2021**, *46*, 100401. https://doi.org/10.1016/j.jphotochemrev.2020.100401.

(68) Ghosh, M.; Mora, A. K.; Nath, S.; Kumar, P. H.; Bangal, P. R.; Sinha, S. Photoinduced Electron Transfer from Zinc Tetraphenylporphyrin to 2-Nitrofluorene in Polar Solvent Acetonitrile. *J. Photochem. Photobiol. Chem.* **2015**, *306*, 55–65. https://doi.org/10.1016/j.jphotochem.2015.03.019.

SYNOPSIS FOR TABLE OF CONTENTS ONLY

The electronic structures of two d^5 metallocenes were investigated via computational and spectroscopic measurements, revealing low-energy LMCT excited states. Coupling these photophysical measurements with ground state thermochemical parameters reveals the promise of these complexes as potent photoreductants with excited state reduction potentials, $[MCp^*_2]^{+/0*}$, greater than –2.6 V vs. $Fc^{+/0}$.

FOR TABLE OF CONTENTS ONLY